2014-11

Calculation of Room Temperature Conductivity and Mobility in Tin-Based Topological Insulator Nanoribbons

UTD AUTHOR(S): William G. Vandenberghe and Massimo V. Fischetti

Vandenberghe, William G., and Massimo V. Fischetti. 2014. "Calculation of room temperature conductivity and mobility in tin-based topological insulator nanoribbons." Journal of Applied Physics 116(17): doi:.10.1063/1.4901063.

Calculation of room temperature conductivity and mobility in tin-based topological insulator nanoribbons

William G. Vandenberghe[a] and Massimo V. Fischetti
Department of Materials Science and Engineering, The University of Texas at Dallas, 800 W Campbell Rd. RL10, Richardson, Texas 75080, USA

(Received 9 August 2014; accepted 24 October 2014; published online 6 November 2014)

Monolayers of tin (stannanane) functionalized with halogens have been shown to be topological insulators. Using density functional theory (DFT), we study the electronic properties and room-temperature transport of nanoribbons of iodine-functionalized stannanane showing that the overlap integral between the wavefunctions associated to edge-states at opposite ends of the ribbons decreases with increasing width of the ribbons. Obtaining the phonon spectra and the deformation potentials also from DFT, we calculate the conductivity of the ribbons using the Kubo-Greenwood formalism and show that their mobility is limited by inter-edge phonon backscattering. We show that wide stannanane ribbons have a mobility exceeding 10^6 cm^2/Vs. Contrary to ordinary semiconductors, two-dimensional topological insulators exhibit a high conductivity at low charge density, decreasing with increasing carrier density. Furthermore, the conductivity of iodine-functionalized stannanane ribbons can be modulated over a range of three orders of magnitude, thus rendering this material extremely interesting for classical computing applications. © *2014 AIP Publishing LLC*. [http://dx.doi.org/10.1063/1.4901063]

I. INTRODUCTION

Recently, it has been shown theoretically that tin in a monolayer buckled hexagonal lattice, which we will hereafter refer to as "stannanane" (from the Latin *stannum* for tin),[1–4] is a two-dimensional topological insulator (TI)[5] also known as quantum spin hall insulator.[6] Stannanane has a predicted bandgap of 100 meV at the K symmetry-point, while functionalization of stannanane with halogens results in bandgaps up to 300 meV at the Γ-point,[7] making stannanane an interesting material for possible room-temperature nanoelectronic applications.

Stannanane has not been experimentally demonstrated yet but when looking at the experimental possibility of realizing monolayer tin, previous literature is encouraging: (i) growth of α-tin, which has a hexagonal lattice along the 111-direction, is stable up to high temperature for thin layers,[8] (ii) binding of halogens with Sn is energetically favorable,[9] (iii) tin can be grown epitaxially on CdTe and InSb substrates,[10] and (iv) monolayers of germanium (germanane) have been grown.[4] Finally, theoretical results show that supported stannanane retains its topological insulating properties and functionalized stannanane is thermodynamically stable with respect to halogen desorption up to high temperature.[11]

Stannanane's topologically non-trivial bandstructure leads to topologically protected edge states. Thanks to time-reversal symmetry, intra-edge elastic backscattering is prohibited, whereas inelastic backscattering is very weak because of the spin-polarization of the edge states.[12,13] The absence of backscattering leads to a quantized conductance (G)[14,15] corresponding to a very high conductivity ($\sigma_{1D} = GL$, L being the length of the insulator), which makes TIs interesting for electronic applications. Of course, in practice scattering with magnetic impurities, the hyperfine interaction,[16] scattering with bulk or other edge states, inelastic scattering, or scattering to the opposite edge will lead to a finite conductivity.

In addition to quantum computing applications,[17,18] TIs could be employed as active elements in classical electronics in two possible ways: (1) as highly conductive interconnects and (2) as a spin-polarizing materials for spintronics.[19]

In this paper, we perform a theoretical study of the upper limit of the conductivity of stannanane as limited by phonon-mediated inter-edge scattering at room temperature. We show that ribbons of TIs have a high conductivity and mobility when the Fermi level lies in the bulk band-gap, but the conductivity decreases as the Fermi level moves out of the bulk band-gap. This high conductivity and the ability to modulate it suggest that two-dimensional TIs can also be of high interest for classical computing even without the need for a nonzero bandgap.[20]

We first calculate the electronic structure of stannanane using density-functional theory (DFT). Then, we calculate the overlap integral between edge states as a function of ribbon-width and wave vector. Next, we calculate the phonon bandstructure and the electron-phonon deformation potentials. We continue by calculating the conductivity and the mobility using the Kubo-Greenwood formalism.[21–23] Finally, we highlight the stark difference between mobility in ordinary semiconductors and TIs and we discuss the potential use of TIs as a future transistor channel-material.

II. ELECTRON AND PHONON BANDSTRUCTURE

The iodostannanane ribbons considered here are illustrated in Fig. 1. Since no experimental bandstructure

[a]wxv101020@utdallas.edu

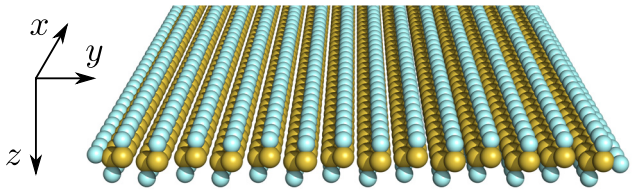

FIG. 1. Illustration of the 14-unitcell zigzag iodostannanane ribbon under study.

parameters are available, we have to rely on the bandstructure obtained from DFT. We use the Vienna *ab initio* simulation package (VASP)[24] with PBE functionals. We choose iodine as a functionalizing element over other halogens because of its lower cut-off energy and the resulting computational convenience. Furthermore, the atomic coordinates are determined by replicating the iodostannanane unit-cell, a number of times depending on the ribbon width and the ribbon is terminated with an iodine atom at both edges. We do not account for substrate effects nor do we relax the free-standing ribbon: maintaining the bulk unit cell in the ribbons enables the use of bulk phonons to calculate the scattering due to the electron-phonon interaction in Sec. III.

The electronic structure of bulk iodostannanane and of a ribbon with a width of 14 unit cells is shown in Fig. 2. Since we consider zigzag ribbons, the bulk dispersion is folded along the Γ- K direction and the ribbon dispersion resembles the bulk dispersion along the Γ- M symmetry line apart from the edge states that close the gap. For very narrow ribbons, a small gap at the Γ-point is maintained because of the inter-edge interaction. The Fermi velocity for the iodostannanane ribbon shown in Fig. 1 is calculated to be $v_F = \mathrm{d}E_{\mathrm{edge}}(k)/\mathrm{d}(\hbar k) \approx 2 \times 10^5$ m/s, which is a little smaller than one half

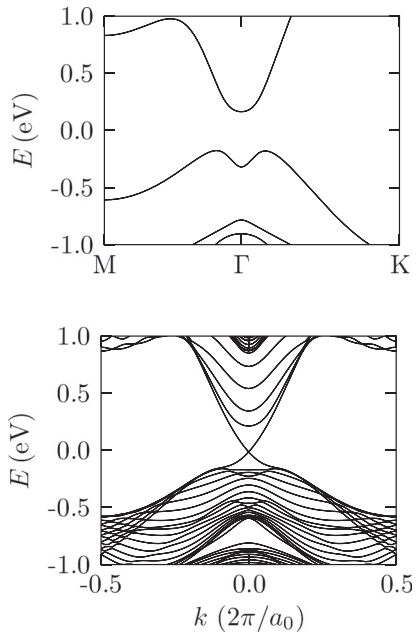

FIG. 2. Calculated bandstructure for bulk iodostannanane (top) and a 14 unit-cell iodostannanane ribbon as illustrated in Fig. 1 (bottom). The ribbon bandstructure resembles the bulk bandstructure folded along the Γ-M direction apart from a 2-fold degenerate band associated with both edges closing the bandgap.

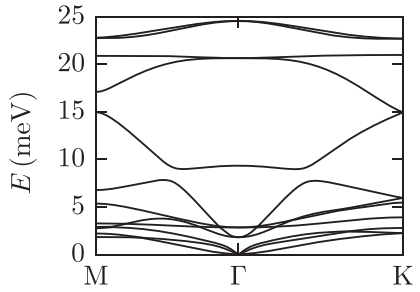

FIG. 3. Phonon bandstructure of bulk iodostannanane.

of the velocity of unfunctionalized stannanane (4.5×10^5 m/s) and one quarter of the Fermi velocity of graphene (10^6 m/s).

To calculate the phonon dispersion, we consider a 3 by 3 bulk iodostannanane supercell using PHONOPY.[25] The force constants for the different atoms in the unit cell are obtained from VASP and the dynamical matrix is computed and diagonalized. The resulting phonon bandstructure is shown in Fig. 3. It should be noted that the phonon energies are much smaller than in graphene because of the higher mass of the tin ions. The sound velocity in ribbons ($v_S = \mathrm{d}\omega/\mathrm{d}k$) is calculated to be 1.4 km/s and 2.3 km/s for the TA and the LA phonons, respectively.

In Fig. 4(a), we show the real-space left- and right-edge (pseudo) wavefunction for $k > 0$. The left-edge state only has a significant spin-down component and its wavefunction quickly decays away from the left edge.[26] In Fig. 4(b), we show the $-k$ wavefunctions to which the $k > 0$ states can backscatter. Because of time-reversal symmetry, the wavefunctions with opposite k are related by the anti-unitary transformation $(\phi_{k\uparrow}, \phi_{k\downarrow})e^{\mathrm{i}kx} \rightarrow (\phi^*_{k\downarrow}, -\phi^*_{k\uparrow})e^{-\mathrm{i}kx}$ so that backscattering to the state on the same edge assisted by a perturbation with time-reversal symmetry is strictly prohibited.

Figure 5 shows the overlap integral of the opposite edge-states as a function of $E_{\mathrm{edge}}(k)$ for different ribbon widths. Obviously, a smaller overlap integral (proportional to the scattering matrix element) yields a smaller backscattering rate and so results in a higher conductivity. As the ribbon width increases, the overlap between the $k > 0$ and $k < 0$ edge states localized at opposite sides decreases. Note that the overlap integral also exhibits a strong dependence on k. Although this dependence is likely to be broadened at room temperature, for $k = 0$, the overlap remains the order of unity. This stems from the inversion-symmetry requirement that the wavefunctions at Γ ($k = 0$) be either fully symmetric or fully antisymmetric, so that the left- and right-edge states cannot be distinguished. Nevertheless, the larger $k = 0$-overlap does not affect the conductivity in any significant way since the small bandgap still present at Γ forces the electron velocity to vanish at $k = 0$ and remain small in the neighborhood of the Γ point. Also note that near $k = 0$, the overlap even exceeds unity since we are treating the projector augmented wavefunctions[27] as pseudopotential wavefunctions.

III. ELECTRON-PHONON INTERACTION

An estimate of the strength of the electron-phonon interaction can be obtained by calculating the deformation

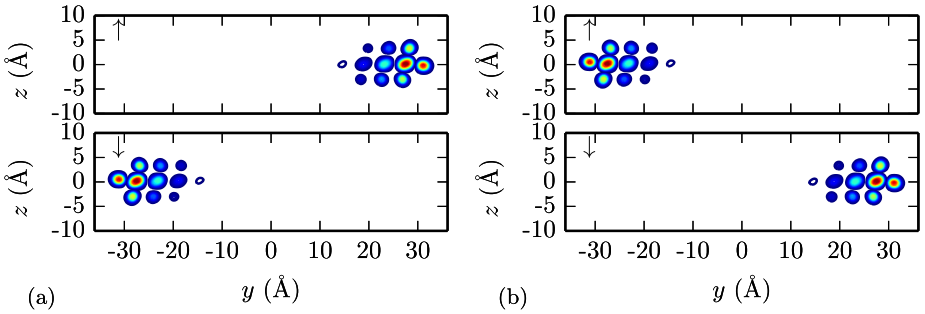

FIG. 4. Illustration of the magnitude of the spin components for both left and right edge states at $k^+ = 0.0025 \times 2\pi/a > 0$ in the conduction band state ($E > 0$) (a) and both the left and right edge states for $k^- = -k^+ < 0$ (b) for the 14-cell wide ribbon. The quantity plotted is the squared magnitude averaged along the x direction (as indicated in Fig. 1) and only areas, where the averaged squared magnitude exceeds 2% of the maximum averaged squared magnitude are colored. The center of the ribbon coincides with the center of the figure. Back-scattering between the left-edge states is prohibited because of time-reversal symmetry but back-scattering between opposite edge states is allowed although strongly suppressed for wide ribbons.

potentials for the conduction band of bulk iodostannanane: The Hartree potential for all independent displacements of each atom in the unit cell is calculated from VASP, as done in Refs. 28–30. Using the electronic wavefunctions and the ionic displacement vectors ($\mathbf{e}^{\nu}_{\mathbf{q},i}$) from the phonon dispersion calculation, where ν is the phonon branch index, $\mathbf{q}$ is the two-dimensional phonon wavevector, and i is the ion index, the deformation potential is calculated from

$$DK^{\nu}_{\mathbf{k},\mathbf{q}} = \sum_{\substack{\mathbf{r} \\ s=\uparrow,\downarrow}} \phi^{*}_{\mathbf{k}+\mathbf{q},s}(\mathbf{r}) e^{i\mathbf{q}\cdot(\mathbf{r}-\mathbf{R}_i)} \phi_{\mathbf{k},s}(\mathbf{r}) \sqrt{\frac{M}{M_i}} \mathbf{e}^{\nu}_{\mathbf{q},i} \cdot \frac{\partial V_{\mathrm{H}}(\mathbf{r})}{\partial \mathbf{R}_i}, \quad (1)$$

where M_i and M are the masses of the ions and of the unit cell, respectively, $V_{\mathrm{H}}(\mathbf{r})$ is the Hartree part of the local potential, and the sum is performed over all positions in a suitable real-space mesh and over both spin components. The largest deformation potential at small momenta is due the phonon branch corresponding to the out-of-phase vibrations of the tin-iodine bond with an energy of 24.5 meV. However, since both the magnitude of the displacement vector and the phonon occupation number are inversely proportional to the phonon frequency, it is the ratio $|DK^{\nu}|^2/(\omega)^2$ that determines which phonons cause the largest scattering rate. In the limit $q \to 0$, this ratio is two orders of magnitude larger for the transverse and longitudinal acoustic phonons than for the optical phonons and for the out-of-plane acoustic

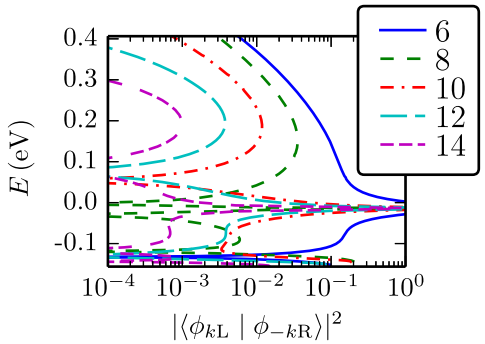

FIG. 5. The wavefunction overlap as a function of energy for different ribbon widths. For most E, the wavefunction overlap decreases exponentially as the ribbon width increases but in a narrow region near $E = 0$ ($k = 0$), where $k \approx -k$, there is no distinction between left- and right edge waves and the overlap is close to unity. On the other hand, the states near $k = 0$ will not affect the conductivity since the electron velocity $\propto \mathrm{d}E/\mathrm{d}k$ vanishes.

phonons. Thus, one has only to consider scattering with transverse and longitudinal acoustic phonons and the computed value for the deformation potentials $D_{\mathrm{LA,TA}} = \mathrm{d}DK/\mathrm{d}q = 27\,\mathrm{eV}$.

The bulk two-dimensional electron-phonon Hamiltonian in the deformation potential approximation reads

$$H_{\mathrm{ep}} = \sum_{\mathbf{q}} D|\mathbf{q}| \sqrt{\frac{\hbar}{WL2\rho\omega_{\mathbf{q}}}} e^{i\mathbf{q}\cdot\mathbf{r}} (\hat{a}(\mathbf{q}) + \hat{a}^{\dagger}(-\mathbf{q})) \quad (2)$$

with D the deformation potential, W and L the ribbon width and length, ρ the two-dimensional mass density, $\omega_{\mathbf{q}}$ the phonon frequency and $a(\mathbf{q})$ and $a^{\dagger}(\mathbf{q})$ phonon annihilation and creation operators. In the elastic approximation, the transition probability due to phonon scattering is

$$W_{k_x k'_x} = \frac{2\pi}{\hbar} \sum_{\mathbf{q}} \frac{\hbar D^2 |\mathbf{q}|^2}{WL2\rho\omega_{\mathbf{q}}} I_{nkn'k'\mathbf{q}} \times \left(1 + 2\nu(\omega_{\mathbf{q}})\right) \delta(E_{nk} - E_{n'k'}) \quad (3)$$

with $I_{nkn'k'\mathbf{q}} = |\langle nk|e^{i\mathbf{q}\cdot\mathbf{r}}|n'k'\rangle|^2$. For the acoustic phonons, $\omega_{\mathbf{q}} \approx v_{\mathrm{s}}|\mathbf{q}|$ and the Bose-Einstein distribution $\nu(\hbar\omega_{\mathbf{q}}) \approx k_{\mathrm{B}}T/\hbar\omega_{\mathbf{q}} \gg 1$, which yields

$$W_{nk_x n'k'_x} \approx \frac{2\pi}{\hbar} \sum_{\mathbf{q}} \frac{D^2 2k_{\mathrm{B}}T}{WL2\rho v_{\mathrm{s}}^2} I_{nkn'k'\mathbf{q}} \delta(E_{nk} - E_{n'k'}). \quad (4)$$

The momentum relaxation rate is computed by

$$\tau_n^{-1}(k) = \sum_{k'_x} W_{nk_x n'k'_x} \frac{v_n(k) - v_{n'}(k')}{v_n(k)} \quad (5)$$

$$= \sum_{\alpha} \frac{2\pi D^2 k_{\mathrm{B}}T}{\hbar\rho_{1\mathrm{D}} v_{\mathrm{s}}^2} \left(\frac{\mathrm{d}E_n(k_x)}{\mathrm{d}k_x}\right)^{-1} \Bigg|_{nk_x=\alpha} \times \frac{v_n(k) - v_{n'}(k')}{v_n(k)} \times \sum_{q_y} \left| \int \mathrm{d}r^3\, u^{*}_{\alpha}(y) e^{iq_y y} u_{nk_x}(y) \right|^2, \quad (6)$$

where α is an index and is summed overall $n'k' \neq nk$, which satisfy $E_{\alpha} = E_{nk}$ and $\rho_{1\mathrm{D}} = \rho W = MN_y/a$ with M the mass of

the unit cell, N_y the number of unit cells in the ribbon and a the unit cell length along the x-direction. For our ribbons, we sum over $q_y = n2\pi/W$ with n going from $-\lfloor (N_y-1)/2 \rfloor$ to $\lfloor N_y/2 \rfloor$; this corresponds to imposing Born-von Karmann boundary conditions on the phonon displacement.

In our calculations, we use $a = 4.9$ Å as the ribbon lattice constant. The momentum relaxation rate is calculated as the sum of a LA and TA scattering rate: $\tau^{-1} = \tau_{\mathrm{LA}}^{-1} + \tau_{\mathrm{TA}}^{-1}$. Each scattering rate $\tau_{\mathrm{TA,LA}}^{-1}$ is calculated with its own deformation potential, $D_{\mathrm{TA,LA}} = 27\,\mathrm{eV}$ and its own sound velocity $v_{\mathrm{LA}} = 1.4\,\mathrm{km/s}$ and $v_{\mathrm{TA}} = 2.3\,\mathrm{km/s}$.

A more rigorous approach of dealing with the phonons would either involve the calculation of the ribbon phonons from first principles or to impose free-floating boundary conditions as is done in Ref. 31. However, the main physics will not be drastically affected and the use of bulk phonons and imposing Born-von Karmann boundary conditions suffices to come to the conclusions of this paper.

IV. CALCULATION OF MOBILITY

In order to evaluate the electron conductivity, we use the Kubo-Greenwood formula

$$\sigma_{1\mathrm{D}} = \frac{2e^2}{k_{\mathrm{B}}T}\sum_j \int \mathrm{d}k\, \tau_j(k) v_j(k)^2 f\big(E_j(k)\big)\big(1 - f\big(E_j(k)\big)\big), \quad (7)$$

where $f(E)$ is the Fermi-Dirac distribution, whose Fermi level E_{F} is taken as a parameter, the temperature T is taken as 300 K, j is the band index, $v_j(k)$ is the electron-velocity computed from the bandstructure as $v_j(k) = \mathrm{d}E_j(k)/\mathrm{d}(\hbar k)$, and the factor 2 results from considering left- and right-edge degeneracy.

In Fig. 6(b), we show the conductivity as a function of the Fermi level, E_{F}. The conductivity increases as the ribbon width increases due to the reduced overlap between the edge states reaching a maximum when the Fermi level is in the bulk band-gap for all ribbons wider than 8 unit cells. However, since the group velocity is higher near the conduction-band minimum than near the valence-band maximum, the largest conductivity is seen when E_{F} is closer to the bulk conduction-band minimum than to the bulk valence-band maximum.

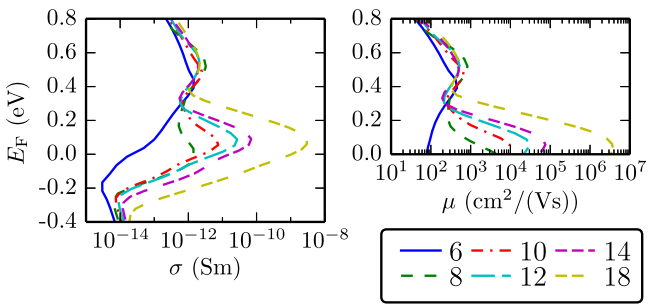

FIG. 6. One-dimensional conductivity and mobility as a function of Fermi level for different ribbon widths, width is expressed in number of unit cells. The conductivity and mobility reach a maximum when the Fermi level lies in the bulk bandgap. For wide ribbons, the mobility is very high and exceeds 10^6 cm^2/Vs.

A more familiar figure-of-merit for electronic performance is the mobility. This can be obtained from the conductivity and the conduction band charge density

$$\mu = \frac{\sigma_{1\mathrm{D}}(E_{\mathrm{F}})}{e\rho_{\mathrm{el,1D}}(E_{\mathrm{F}})} \quad \text{and} \quad \rho_{\mathrm{el,1D}} = \int \frac{\mathrm{d}k}{2\pi} f(E_{\mathrm{c}}(k)). \quad (8)$$

Figure 6 shows that the phonon-limited mobility of iodostannanane for the widest ribbon exceeds the graphene mobility $\approx 10^6$ cm^2/Vs.[32]

With these high conductivities and mobilities, it is important to remember that competing scattering processes such as impurity scattering or edge-roughness scattering will also be strongly suppressed for wide ribbons. But the current in iodostannanane will also never exceed the ballistic limit and for short ribbons, conductance rather conductivity will limit the current. Nevertheless, as ribbon lengths increase, diffusive transport will always dominate.

The physical processes that control the electron-phonon-limited conductivity in 2D TI ribbons differ sharply from those that control the conductivity of conventional semiconductors. In ordinary semiconductors, the conductivity is approximately linearly proportional to the density of free carriers, n, via $\sigma = ne\mu$, and the mobility is mainly determined by the electron velocity (in addition to the scattering rates, obviously). In 2D TIs, instead, the conductivity is determined by inter-edge scattering and so by the overlap factor, resulting in a behavior that is extremely (exponentially) sensitive to the width of the ribbon. Furthermore, as the Fermi level increases towards the conduction-band minimum, the free-carrier density in the conduction band increases but, simultaneously, the carrier velocity decreases and scattering towards bulk states becomes possible, effects that suppress the conductivity. Therefore, in TIs, the conductivity is inversely proportional to the charge density.

When considering TIs for transistor applications, it is important to remember the great strength of semiconductors: the ability to modify charge density over many orders of magnitude with a small change in bias. Ideally, for every $\log(10)kT/e$ change in Fermi level, the charge density changes by an order of magnitude. Since the conductivity of semiconductors is linearly proportional to the charge concentration, the conductivity can also be changed over many orders of magnitude. Thus, viewing this from a topological perspective, it is possible to change an ordinary semiconductor from an insulator to a metal by applying an external bias and so moving the Fermi level into the conduction band. This is exactly the basic working principle of the Metal-oxide-semiconductor field-effect transistor (MOSFET).

Here, we have demonstrated a similar concept: The mobility of TI ribbons is also strongly (exponentially) dependent on the position of the Fermi level, although in the opposite way, and it is possible to modulate the conductivity over 3 orders of magnitude. This finding opens the idea of a TI-based MOSFET in which a transition from a low- to high-conductivity state can be obtained by shifting the Fermi level towards the middle of the TI bulk band-gap via the gate bias. A possible advantage of this alternative gating scheme consists in the fact that only a small amount of charge needs

to be displaced to obtain the highly conductive state, thus suggesting high-speed switching thanks to the high velocity of the charge carriers.

V. CONCLUSION

Using DFT, we have computed the electronic and phonon bandstructure for iodostannanane ribbons. While intra-edge backscattering is prohibited because of the spin-polarization of the edge-states, the wavefunction overlap characterizing inter-edge backscattering was calculated and shown to be reducing exponentially with ribbon width. The conductivity was calculated using the Kubo-Greenwood formalism and was shown to be very high. Along with the conductivity, the mobility was calculated as well and in wide ribbons, the mobility even exceeded 10^6 cm^2/Vs. At the same time, we have shown that the conductivity is also strongly dependent on the position of the Fermi level. And the ability to modulate the conductivity opens up the possibility of using topological insulators for transistor applications.

ACKNOWLEDGMENTS

We thank Yong Xu and Robert Wallace for useful discussions and we acknowledge the support of Nanoelectronics Research Initiative's (NRI's) Southwest Academy of Nanoelectronics (SWAN).

[1]We deviate from a previous naming of two-dimensional tin as "stanene" to highlight the sp^3 hybridization of the tin. The naming of monolayer tin as stannanane further differentiates it from stannane (SnH_4) and is also in line with the naming of other buckled group IV monolayers such as graphane, silicane, and germanane.

[2]D. C. Elias, R. R. Nair, T. M. G. Mohiuddin, S. V. Morozov, P. Blake, M. P. Halsall, A. C. Ferrari, D. W. Boukhvalov, M. I. Katsnelson, A. K. Geim *et al.*, "Control of graphene's properties by reversible hydrogenation: Evidence for graphane," Science **323**(5914), 610–613 (2009).
[3]M. Houssa, G. Pourtois, V. V. Afanasev, and A. Stesmans, "Can silicon behave like graphene? A first-principles study," Appl. Phys. Lett. **97**(11), 112106 (2010).
[4]E. Bianco, S. Butler, S. Jiang, O. D. Restrepo, W. Windl, and J. E. Goldberger, "Stability and exfoliation of germanane: A germanium graphane analogue," ACS Nano **7**(5), 4414–4421 (2013).
[5]Y. Xu, B. Yan, Hai-Jun Zhang, J. Wang, G. Xu, P. Tang, W. Duan, and Shou-Cheng Zhang, "Large-gap quantum spin Hall insulators in tin films," Phys. Rev. Lett. **111**(13), 136804 (2013).
[6]C. L. Kane and E. J. Mele, "Quantum spin Hall effect in graphene," Phys. Rev. Lett. **95**(22), 226801 (2005).
[7]Y. Ma, Y. Dai, M. Guo, C. Niu, and B. Huang, "Intriguing behavior of halogenated two-dimensional tin," J. Phys. Chem. C **116**(23), 12977–12981 (2012).
[8]R. F. C. Farrow, D. S. Robertson, G. M. Williams, A. G. Cullis, G. R. Jones, I. M. Young, and P. N. J. Dennis, "The growth of metastable, heteroepitaxial films of α-sn by metal beam epitaxy," J. Cryst. Growth **54**(3), 507–518 (1981).
[9]S. Ciach, D. J. Knowles, A. J. C. Nicholson, and D. L. Swingler, "Vaporization of tin (ii) halides. i. stannous chloride and stannous bromide," Inorg. Chem. **12**(6), 1443–1446 (1973).
[10]P. Fantini, S. Gardonio, P. Barbieri, U. del Pennino, C. Mariani, M. G. Betti, E. Magnano, M. Pivetta, and M. Sancrotti, "α-sn pseudomorphic growth on InSb (111) and (111) surfaces: A high-resolution photoemission study," Surf. Sci. **463**(3), 174–182 (2000).
[11]A. S. Negreira, W. G. Vandenberghe, and M. V. Fischetti, "Ab initio study of the electronic properties and thermodynamic stability of supported 2d-sn (stannanane) films," (in preparation).
[12]T. L. Schmidt, S. Rachel, F. von Oppen, and L. I. Glazman, "Inelastic electron backscattering in a generic helical edge channel," Phys. Rev. Lett. **108**(15), 156402 (2012).
[13]J. C. Budich, F. Dolcini, P. Recher, and B. Trauzettel, "Phonon-induced backscattering in helical edge states," Phys. Rev. Lett. **108**(8), 086602 (2012).
[14]B. A. Bernevig and Shou-Cheng Zhang, "Quantum spin Hall effect," Phys. Rev. Lett. **96**(10), 106802 (2006).
[15]M. König, S. Wiedmann, C. Brüne, A. Roth, H. Buhmann, L. W. Molenkamp, Xiao-Liang Qi, and Shou-Cheng Zhang, "Quantum spin Hall insulator state in Hg Te quantum wells," Science **318**(5851), 766–770 (2007).
[16]A. M. Lunde and G. Platero, "Hyperfine interactions in two-dimensional Hg Te topological insulators," Phys. Rev. B **88**(11), 115411 (2013).
[17]L. Fu and C. L. Kane, "Probing neutral majorana fermion edge modes with charge transport," Phys. Rev. Lett. **102**(21), 216403 (2009).
[18]J. E. Moore, "The birth of topological insulators," Nature **464**(7286), 194–198 (2010).
[19]D. Pesin and A. H. MacDonald, "Spintronics and pseudospintronics in graphene and topological insulators," Nat. Mater. **11**(5), 409–416 (2012).
[20]J. Chang, L. F. Register, and S. K. Banerjee, "Topological insulator Bi_2Se_3 thin films as an alternative channel material in metal-oxide-semiconductor field-effect transistors," J. Appl. Phys. **112**(12), 124511 (2012).
[21]D. A. Greenwood, "The boltzmann equation in the theory of electrical conduction in metals," Proc. Phys. Soc. **71**(4), 585 (1958).
[22]B. Soree, W. Magnus, and W. Vandenberghe, "Low-field mobility in ultra-thin silicon nanowire junctionless transistors," Appl. Phys. Lett. **99**(23), 233509 (2011).
[23]J. Kim, M. V. Fischetti, and S. Aboud, "Structural, electronic, and transport properties of silicane nanoribbons," Phys. Rev. B **86**(20), 205323 (2012).
[24]G. Kresse and J. Hafner, "Ab initio molecular dynamics for liquid metals," Phys. Rev. B **47**(1), 558 (1993).
[25]A. Togo, F. Oba, and I. Tanaka, "First-principles calculations of the ferroelastic transition between rutile-type and $CaCl_2$-type SiO_2 at high pressures," Phys. Rev. B **78**(13), 134106 (2008).
[26]B. Zhou, Hai-Zhou Lu, Rui-Lin Chu, Shun-Qing Shen, and Q. Niu, "Finite size effects on helical edge states in a quantum spin-Hall system," Phys. Rev. Lett. **101**(24), 246807 (2008).
[27]P. E. Blöchl, "Projector augmented-wave method," Phys. Rev. B **50**(24), 17953 (1994).
[28]K. M. Borysenko, J. T. Mullen, E. A. Barry, S. Paul, Y. G. Semenov, J. M. Zavada, M. B. Nardelli, and K. W. Kim, "First-principles analysis of electron-phonon interactions in graphene," Phys. Rev. B **81**, 121412 (2010).
[29]K. Kaasbjerg, K. S. Thygesen, and K. W. Jacobsen, "Phonon-limited mobility in n-type single-layer MoS_2 from first principles," Phys. Rev. B **85**(11), 115317 (2012).
[30]W. G. Vandenberghe and M. V. Fischetti, "Calculation of electron-phonon interaction strength from first principles in graphene and silicon," in *Proceedings of the 2014 International Workshop on Computational Electronics (IWCE)* (IEEE, 2014), pp. 1–2.
[31]N. Bannov, V. Mitin, and M. Stroscio, "Confined acoustic phonons in a free-standing quantum well and their interaction with electrons," Phys. Status Solidi B **183**(1), 131–142 (1994).
[32]K. I. Bolotin, K. J. Sikes, Z. Jiang, M. Klima, G. Fudenberg, J. Hone, P. Kim, and H. L. Stormer, "Ultrahigh electron mobility in suspended graphene," Solid State Commun. **146**(9), 351–355 (2008).